Kan et al. *NPG Asia Materials* (2025)17:38
https://doi.org/10.1038/s41427-025-00619-2

NPG Asia Materials

ARTICLE Open Access

Colossal barocaloric effect in $GdCl_3$-doped H_2O for sustainable cooling

Yue Kan[1,2], Feng-Xia Hu[1,2,3], Jian-Tao Wang[1,2,3], Jia-Zheng Hao[4], Qiang Li[5], Yi-Li Cao[5], Fei-Ran Shen[4], Wen Yin[4], Lun-Hua He[1,3,4], Bo Su[1,2], Jing Wang[1,2], Ji-Rong Sun[1,2], Zhi-Guo Chen[1,2], Chang-Qing Jin[1,2], Xian-Ran Xing[5], Yun-Zhong Chen[1,2], Tong-Yun Zhao[1,6], Wei Zhai[7], Bing-Bo Wei[7] and Bao-Gen Shen[1,2,6,8]

Abstract

H_2O exists everywhere and its huge latent heat across ice-water phase transition empowers it to be a potential candidate for barocaloric refrigeration applications. Here we report a colossal and reversible barocaloric effect (BCE) in doped H_2O, where the large hysteresis caused by supercooling is solved by adding 1.33 wt% $GdCl_3$. Thereby the reversible entropy change $\Delta S_r \sim 728\ J\ kg^{-1}\ K^{-1}$ has been demonstrated under a low pressure of 0.1 GPa and a more attractive colossal one ($1018\ J\ kg^{-1}\ K^{-1}$) can be achieved at 0.16 GPa, exceeding those of all other BCE materials and most of the harmful Freon in vapor compression refrigeration. Neutron measurements combined with molecular dynamics simulations demonstrated that the colossal BCE originates from the breakage/formation of H-bonds in H_2O. Phonon density of states and Raman spectra validate the change of H-bonds from perspective of dynamics. The super BCE performance and the ubiquitous, non-toxic characters make H_2O attractive as barocaloric refrigerant for sustainable cooling, more importantly, it is inferred that H-bond engineering can be an attractive approach for designing novel caloric materials.

Introduction

Refrigeration is ubiquitous in our daily life, either food storage and medical treatment, or air conditioners and all kinds of electronic devices, it can be found almost everywhere[1]. With the inexorable development of technology and civilization, the consumption of electricity is increasing in an astonishing speed, nearly 25% of which is attributed to the refrigeration field[2]. The current refrigerants used in this technology are mostly harmful gases like hydrofluorocarbon-which have global warming potentials exceeding 2000 times that of CO_2 and hence is unfriendly to our planet[3,4]. Therefore, there is an urgent need to develop a brand-new environmentally benign and efficient refrigeration technology to address this issue[5].

Under such a circumstance, solid-state refrigeration based on caloric effect from phase transition is likely to undertake this arduous task[6]. Caloric effect can be categorized into barocaloric effect (BCE)[7–14], magnetocaloric effect (MCE)[15–17], electrocaloric effect (ECE)[18–21], and elastocaloric effect (eCE)[22,23], among which BCE attracts an increasing attention because of its universality, safety and relative low cost compared with the expensive magnetic field of MCE, the breakdown voltage of ECE and the demand of huge mechanical strength of eCE materials. In contrast, it is relatively easy to obtain a hydrostatic pressure through pressure-transmitting mediums[24–26]. In fact, BCE has been found in a broad range of materials, such as spin-crossover materials[27–29], solid-liquid phase transition n-alkanes[30,31], plastic crystals[25,32–36], ferro/ferrielectric materials[37,38], ferroelastic materials[39], organic-inorganic materials with carbon chains[40], and magnetic phase transition alloys[41–45].

The past few years have witnessed the thriving of the BCE materials, especially the discovery of organic plastic crystal with barocaloric entropy change (ΔS) more than $500\ J\ kg^{-1}\ K^{-1}$, which indeed offered a strong impulse in this field[32]. Moreover, giant BCE with ΔS more than $100\ J\ kg^{-1}\ K^{-1}$ has been also found in many other materials

Correspondence: Feng-Xia Hu (fxhu@iphy.ac.cn) or Jian-Tao Wang (wjt@iphy.ac.cn) or Jing Wang (wangjing@iphy.ac.cn) or Bao-Gen Shen (shenbg@iphy.ac.cn)
[1]Beijing National Laboratory for Condensed Matter Physics, Institute of Physics, Chinese Academy of Sciences, Beijing, PR China
[2]School of Physical Sciences, University of Chinese Academy of Sciences, Beijing, PR China
Full list of author information is available at the end of the article

and ΔS with ~720 J kg^{-1} K^{-1} was found in n-alkanes associated with solid–liquid phase transition[30,31]. However, the materials with huge ΔS are commonly organic ones, which can be more or less toxic and need to be chemically synthesized.

Herein, we exploit H_2O as the target candidate, which has been overlooked, for the study of BCE after taking a few merits into account. First, H_2O is ubiquitous; second, the latent heat of the ice-water phase transition around 273 K is huge, ~340 kJ/kg from our measurements, and the corresponding entropy change ΔS is ~1200 J kg^{-1} K^{-1}, also accompanied with a maximal isothermal entropy change ΔS_{iso}~1050 J kg^{-1} K^{-1} at a small pressure of 0.1 GPa, which is hitherto, to the best of our knowledge, the highest value among the reported BCE and the only one more than 1000 J kg^{-1} K^{-1}. Moreover, reversible barocaloric entropy change as much as 1018 J kg^{-1} K^{-1} can be achieved by significantly mitigating supercooling degree through adding a little amount of dopant (1.33 wt% $GdCl_3$). While the reversible refrigeration capacity RC_{rev} which represents the capacity for exchanging heat between hot and cold sink in an ideal cooling cycle can reach 9700 J/kg, at the tier 1 place among the reported BCE materials. H_2O is environmentally benign, harmless and non-toxic, hence it is likely to be a satisfactory and potential candidate for BCE refrigeration.

During exploring colossal BCE in H_2O associated with the transition between crystalline ice-I_h and disordered water, a few new findings emerged. Our neutron studies presented the first experimental evidence that the main cause of H-bond breakage during ice-water transition is the O-H bending instead of the elongation of O-O distance between neighboring molecules (which was once predicted via simulation[46] but no experimental evidence was given so far), from which the critical cutoff value of H-bonds was firstly determined. On the basis, the exact coordination number of H-bonds in ice and water was obtained by combining with DFT-MD calculations, i.e. 4/molecule at ice declines to 3/molecule at water in average, which was validated by our experiments considering the H-bond energy from x-ray absorption spectrum (XAS)[47]. This result not only explains the colossal BCE from H-bonds in H_2O, more importantly, it provides robust enlightenment that H-bond engineering would be a feasible method to produce more attractive colossal entropy change by creating stronger H-bonds and/or increasing the number of them. This is distinct from the mechanism of complicated organic materials, where the changes of conformation ordering and/or molecular orientation are responsible for the colossal BCE. Besides, an important side finding is the direct experimental evidence of the gas clathrate into ice crystal, which infers the probability of creatures' existence even in ice and delights people to explore new lives in extreme geological environment.

Results

Barocaloric performances

The H_2O sample used in the heat flow measurements was sterile double-distilled H_2O to confirm its purity and obtain more accurate results. The heat flow results for pure H_2O at ambient pressure with a temperature ramping rate of 1 K/min are shown in Fig. 1a. The sample clearly shows a first-order phase transition with sharp heat flow peaks on heating/cooling, with transition temperatures of approximately 275.4 K/257.1 K, accompanied by a hysteresis of approximately 18.3 K (defined as the temperature difference between the heat flow peaks) owing to the supercooling effect (see details given in Supplementary Note S2). The corresponding entropy change related to the phase transition was ~1170 J kg^{-1} K^{-1}, which is a record-high value to date among all published BCE materials and also larger than the entropy change of vaporization of R1234yf ($CF_3CH_2CF_3$, 741 J kg^{-1} K^{-1})[48] and R1234ze(E) (CHF = $CHCF_3$ (trans), 727 J kg^{-1} K^{-1})[49], which are environmentally harmful hydrofluorocarbons and hydrofluoroolefins used in conventional vapor compression refrigeration technologies (Supplementary Table S5)[50]. Therefore, with such an enormous entropy change, a superior BCE can be expected from H_2O.

First, we studied the BCE of pure H_2O by high-pressure DSC under various pressures. The peaks of melting/freezing were confirmed to be 275.4 K/257.1 K at atmospheric pressure and 266.1 K/245.0 K at 0.1 GPa with nearly the same thermal hysteresis ~18 K (Fig. S1a). The pressure sensitivity can be deduced to be $dT_c/dP = -122$ K/GPa and −92 K/GPa for cooling and heating, respectively (Fig. S1c), in line with the trend shown in the three-phase diagram (Fig. S25b)[51]. Accordingly, the entropy change across the solid-liquid phase transition could be extracted for all applied pressures. The entropy change across the phase transition slightly declined from 1170 J·kg^{-1}·K^{-1} at atmospheric pressure to 1050 J·kg^{-1}·K^{-1} at 0.1 GPa (Fig. S3a, b) owing to the complexation of H_2O with the pressure transmitting gas (Figs. S18 and S19, Supplementary Note S5). Next, the pressurization induced isothermal entropy change (ΔS_{iso}) was calculated according to the equation ΔS_{iso} (T, $P_1 \rightarrow P_2$) = S (T, P_2) − S (T, P_1), where the atmospheric pressure was set to be the initial and terminal pressure for the compression and decompression procedure, respectively, and the results are plotted in Fig. 1c. The barocaloric entropy change reached a maximum of ΔS_{iso} ~1050 J·kg^{-1}·K^{-1} under a small pressure of 0.10 GPa under pressurization and depressurization respectively.

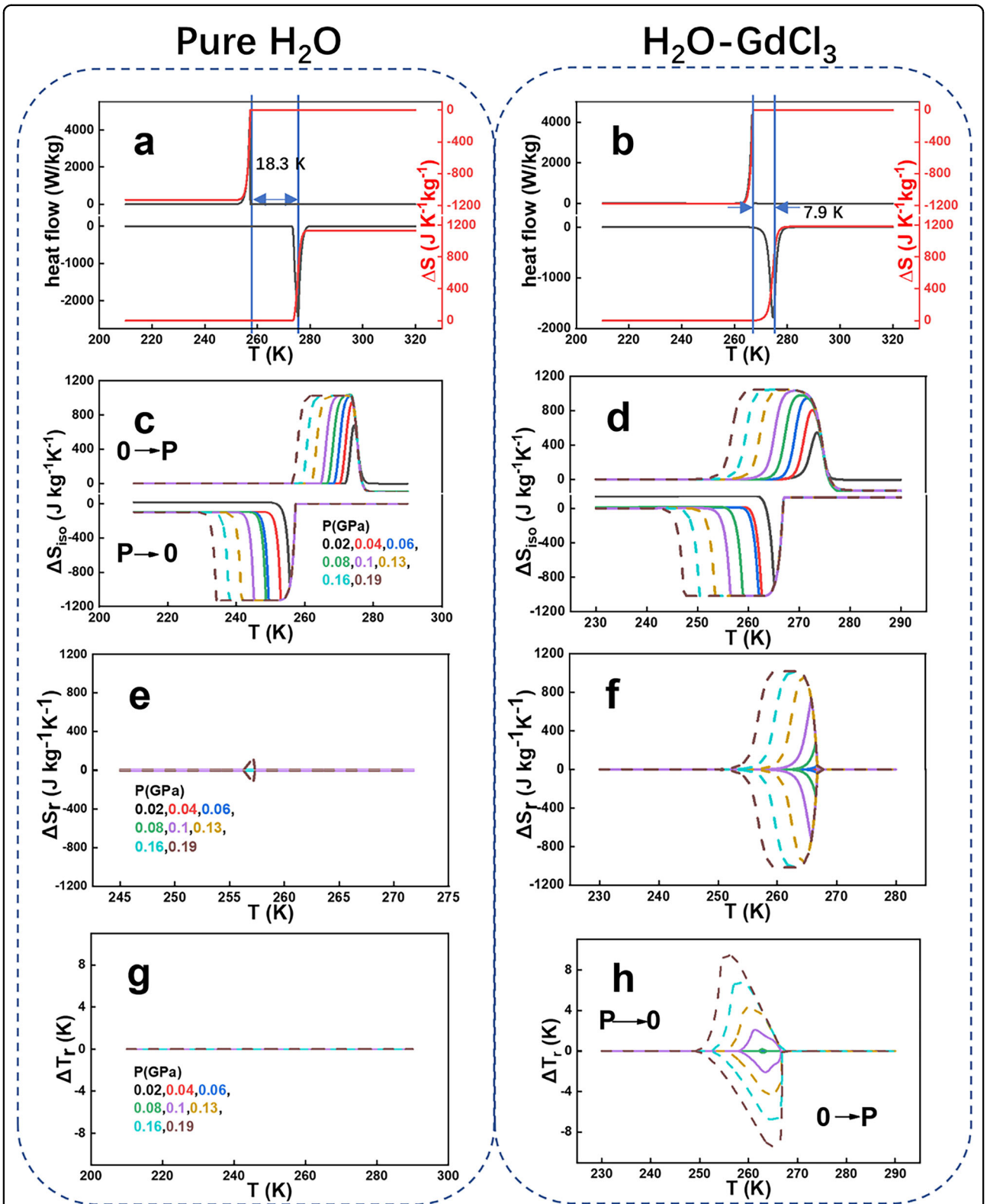

Fig. 1 Barocaloric performance of pure H_2O and with 1.33 wt% $GdCl_3$ addition. a Heat flow measured at atmospheric pressure with a temperature ramping rate of 1 K/min for pure H_2O and **b** H_2O with $GdCl_3$. **c** Isothermal entropy change ΔS_{iso} induced by compression (upside) and decompression (downside) of pure H_2O and **d** H_2O with $GdCl_3$. **e** Reversible entropy change ΔS_r under various pressures for pure H_2O and **f** H_2O with $GdCl_3$. **g** Reversible adiabatic temperature change from cooling entropy curve at atmospheric pressure and heating entropy curves under applied pressure for pure H_2O and **h** H_2O with $GdCl_3$. The extrapolating curves are plotted by dashed lines.

This barocaloric ΔS_{iso} is huge; however, only the reversible parts of the entropy change and adiabatic temperature change, i.e., ΔS_r and ΔT_r, contribute substantially to practical refrigeration. We further investigated the reversibility of the BCE. The reversible ΔS_r was obtained from the overlapping pressurization- and depressurization-induced isothermal entropy change. As shown in Fig. 1c, there was no overlap between the two areas up to 0.1 GPa and no reversible ΔT_r; in other words, pure H_2O cannot be applied in practical BCE cooling up to 0.1 GPa.

Limited to the pressure of our high-pressure DSC apparatus, we cannot perform heat flow measurement at higher pressures. Fortunately, the dT_c/dP of H_2O is almost linear (Fig. S1c, d, and Fig. S25, the three-phase diagram of H_2O) such that extrapolation can be used to predict ΔS_{iso} at higher pressures, as shown in Fig. S3a, b and Supplementary Note S10 (the dotted lines), from which the reversible ΔS_r can be determined (Fig. 1e). Even when the applied pressure reached 0.19 GPa, ΔS_r had a tiny value of 160 $J{\cdot}kg^{-1}{\cdot}K^{-1}$ whereas the reversible ΔT_r was still zero (Fig. 1g). These BCE performances are likely to be disappointing considering the three-phase diagram of H_2O (Fig. S25b)[51], where there is an inflection point at approximately 0.22 GPa and the dT_c/dP changes to be positive instead of negative, such that the pressure range should not surpass this value to obtain a BCE.

The bottleneck is that the giant entropy change ΔS cannot be reversibly driven owing to the large hysteresis (~18.3 K) caused by the supercooling effect for pure H_2O. Fortunately, the supercooling degree, i.e., the hysteresis gap, can be mediated by doping[52–54]. After testing a range of dopants (including monovalence, divalence and trivalence metal ions and insoluble matters), where $GdCl_3$ behaves the best, then a 1.33 wt% ratio of $GdCl_3$ was eventually chosen to further explore the BCE of doped H_2O. (Fig. 2 and Supplementary Note S3) The measurement conditions were the same as those used for the pure H_2O and the results are illustrated in the right part of Fig. 1. The barocaloric ΔS_{iso} remained the same as that of pure H_2O (Fig. 1d) (Supplementary Note S4); however, the thermal hysteresis decreased to ~7.9 K (Fig. 1b, d), which is narrower than that of some well-known plastic crystals such as NPG, PG, and AMP[25,32,33] and solid-liquid phase transition n-alkanes[30] with huge latent heat ever reported as BCE materials. The relative mechanism of dopants reducing hysteresis can be seen in Supplementary Note S3. From Fig. 1d, it can be seen that there has already been overlapped areas between the pressurization induced ΔS_{iso} at 0.1 GPa and the depressurization caused one at 0.1 GPa. Accordingly, the reversible isothermal entropy change ΔS_r is shown in Fig. 1f by extrapolating pressure up to 0.19 GPa, guaranteeing not to surpass the pressure inflection point in three-phase diagram (Fig. S25b)[51]. $\Delta S_r \sim 1018\ J{\cdot}kg^{-1}{\cdot}K^{-1}$ is obtained at 0.16 GPa, which is hitherto the record-high reversible entropy change among all reported BCE materials. The related adiabatic temperature change was also attained considering the entropy change contribution from the specific heat capacity (see Supplementary Note S1 and Figs. S4–S6). The calculated adiabatic temperature change from the quasi-direct method showed a peak value of $\Delta T_{ad} \sim$ -17 K/19 K upon pressurization/depressurization at 0.19 GPa (Fig. S1f), whereas the reversible ones were $\Delta T_r \sim$ -9.4 K (Fig. 1h). Moreover, the cooling performances of barocaloric effects can also be assessed by the reversible refrigeration capacity ($RC_{rev} = \Delta S_{r,max}{}^{*}\Delta T_{FWHM}$) which takes into account not only the maximal reversible entropy change $\Delta S_{r,max}$ but also the temperature span range ΔT_{FWHM} (the full width at the half maximum of the ΔS_r curves) so this parameter would be more comprehensive when evaluating actual performance. RC_{rev} denotes the heat transfer capacity from cold to hot reservoir in a reversible refrigeration cycle. As shown in Fig. S31, the RC_{rev} can reach 9700 J/kg at 0.19 GPa, strongly indicating high potential for actual refrigeration applications. Such a value is quite large after comparing H_2O-1.33 wt% $GdCl_3$ with other famous candidates. Moreover, in terms of the RC_{rev} obtained under certain pressure, the parameter RC_{rev}/P of H_2O-1.33 wt% $GdCl_3$ is still at the tier 1 place amongst the listed candidates with a high value of 51052 $J{\cdot}kg^{-1}GPa^{-1}$ (see Figs. S31, S32, Table 2), further confirming the accessibility of the cooling potential from H_2O-1.33 wt% $GdCl_3$.

Neutron diffraction

To understand the mechanism of so huge an entropy change during phase transition, neutron diffraction (ND) and pair distribution function (PDF) measurements were performed to unveil the structural evolution and dynamics of the local atomic environment of H_2O. To obtain a high signal to noise ratio, H was substituted with D in the ND experiment. From the ND result at 180 K (Fig. 3a and Fig. S2), the structure and lattice parameters of hexagonal ice ($P6_3/mmc$) were determined (Supplementary Table S4), consistent with the three-phase diagram[51,55,56]. As the temperature was increased to 230 K but remained below T_C (277 K), the ND pattern remained the same with clearly visible diffraction peaks (Fig. S2d and e). However, at 300 K, above the T_C, there were no diffraction peaks but rather a broadened feature (Fig. 3c), which is a typical character of a disordered phase.

Pair distribution function (PDF) analysis

To detect the specific molecule movements and dynamics of local atomic environments, we further performed neutron PDF analysis, with the use of Bragg and diffuse scattering. The PDF results, shown in Fig. 4a,

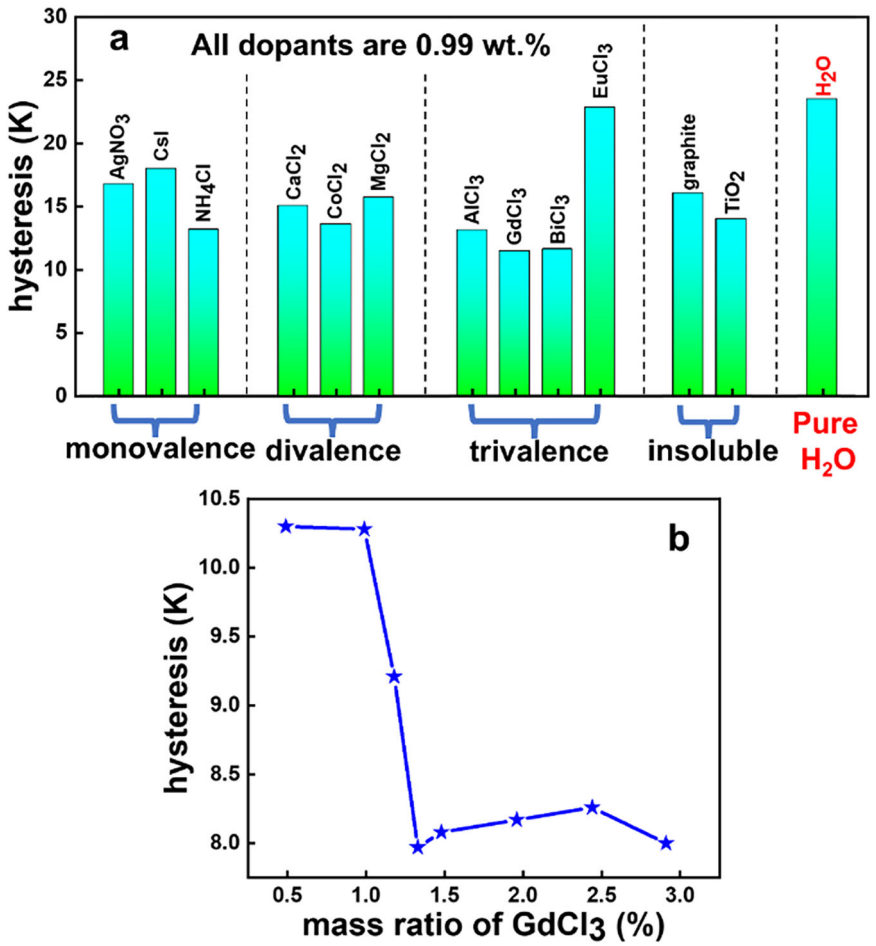

Fig. 2 Hysteresis of H_2O. a after addition of diverse dopants (including monovalence, divalence and trivalence metal ions and insoluble matters) with the same concentration 0.99 wt% and **b** various mass ratios of $GdCl_3$. Temperature scanning rate is 1 K/min.

reveal a conspicuous difference between the results at 300 K (liquid water) and those at 180 and 230 K (ice form). For d > 5 Å, all sharp peaks once discernable at 180 K and 230 K become invisible at 300 K, reflecting highly disordering of liquid water. To elaborately analyze the specific changes in the atomic local environment from ice to water, we then focused on the first 5 peaks (Fig. 4b), which correspond to the intramolecular and intermolecular (1) O-D, (2) D-D, (3) D-O, (4) D-D, and (5) O-O pairs (Fig. 4b, c). The remarkable decrease of peak intensity and area on transitioning from ice to water, particularly for peaks (3), (4), and (5) from the intermolecular pairs, unambiguously conveys that the coordination number of D_2O molecules decreased. It means that the number of neighboring molecules bonded with a certain individual D_2O molecule decreased and the local environment became more disordered in liquid water. Specifically, the peak (3) (inter D-O), denoting the H-bond connecting two neighboring D_2O molecules, markedly shifted to a higher d value compared with the other 4 peaks (Table 1), which indicates that the H-bonds were markedly elongated in liquid water.

More accurately, the positions of peak (3) (inter D-O) in ice and liquid water are 1.765 Å and 1.865 Å, respectively, with an elongation $\Delta d_{O\text{-}D} = 0.1$ Å. Meanwhile, the peak (5) (inter O-O) at 2.745 Å in ice, along with the peak (4) (inter D-D) at 2.315 Å, slightly change to 2.755 Å and 2.325 Å respectively in liquid water with an extension of only $\Delta d_{O\text{-}O} = 0.01$ Å, 1/10 of the value of the peak (3) (inter D-O). Under such a circumstance to satisfy the geometric relationship, the intra O-D bond needs to rotate around the intra O atom in a molecule when it transforms from ice to liquid water, as illustrated in Fig. 4e, where a non-zero angle θ (defined as the O-O-D angle) emerges in water that was absent in the ice phase. It is mainly due to this rotation of the intra O-D bond instead of the separation of the two neighboring molecules that causes elongation of the nearest O-D distance (i.e., the H-bond between two neighboring H_2O

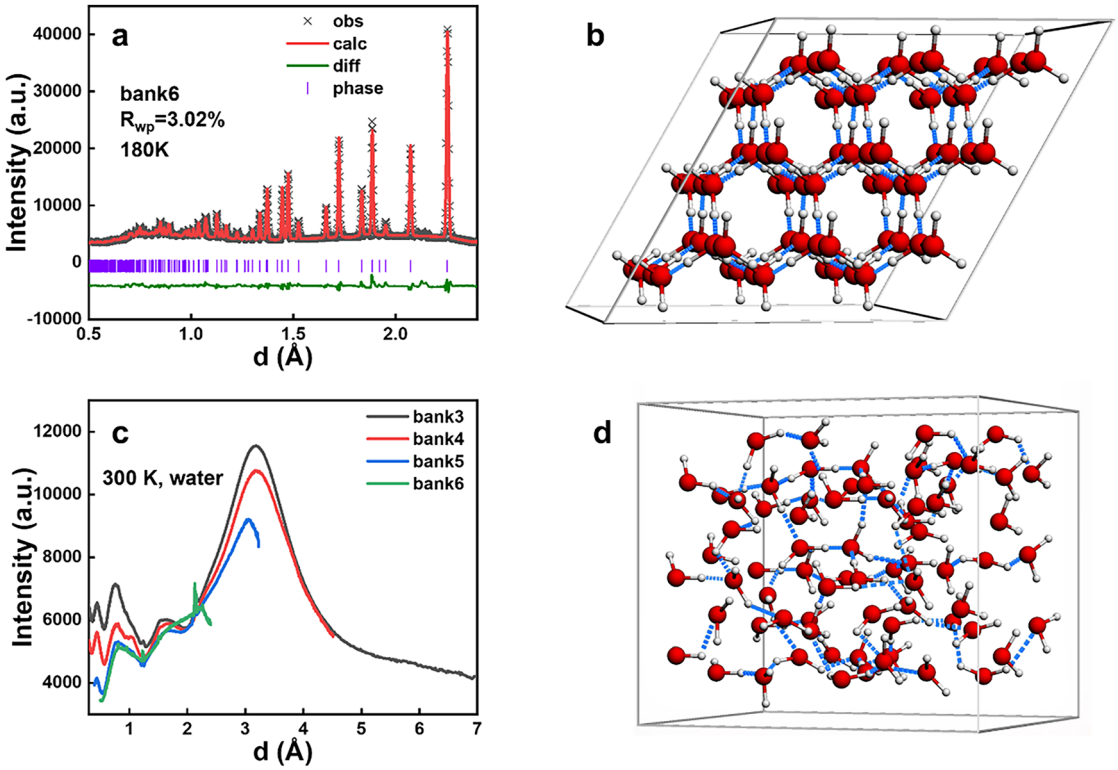

Fig. 3 ND results of D_2O. a Refinement ND results of bank 6 at 180 K. **b** Schematic diagram of ice crystal form. **c** ND raw data at 300 K. **d** Schematic diagram of liquid water. Red and white balls denote O and H atoms, respectively, while the dotted blue lines mark H-bonds connecting two H_2O molecules.

molecules), eventually inducing impairment of the H-bonds. That is, the breakage of H-bonds across the ice-water phase transition is caused by rotation of the molecule around its own O atom, which experimentally evidences the long-standing speculations in previous literature[46], where Wernet et al. by theoretical simulation predicted that the H-bonds are predominantly broken by bending of a certain H_2O molecule rather than by elongation between neighboring molecules, but no experimental evidence was given so far. Moreover, the three atoms O-O-D after rotation form a triangle and the length of three sides can be obtained (Fig. 4e), with $r_{O\text{-}O} = 2.755$ Å, $r_{O\text{-}H,inter} = 1.865$ Å and $r_{O\text{-}H,intra} = 0.975$ Å at 300 K, and then the O-O-D angle θ~19.55° can be straightforwardly determined. It is noteworthy that these results are obtained via the PDF peak positions accompanied with peak width, which means the uncertainty or fluctuation of the atom pairs involving disorder, reflected by the significant decrease of the peak intensity and broadening of the peak width across ice-water transition, particularly for the intermolecular pairs, i.e. peaks (3), (4) and (5). That is to say, the illustration in Fig. 4e denotes the "average" situation, whereas the real-world environment is more complex and diverse.

Molecular dynamics simulations

To make a quantitative characterization on H-bonds responsible for the colossal entropy change across the phase transition, we performed molecular dynamics (MD) simulations of the H-bonds based on density functional theory (DFT) and the outcomes of the above PDF analysis. In fact, the H-bonds in liquid water is continuously broken and reformed, i.e., liquid water is a dynamic system[57] and the H_2O molecules can form diverse polyhedrons at a certain time and then disintegrate immediately, before constituting another arbitrary polyhedron again[58,59]. Here, for simplicity, 72 H_2O molecules were considered using two independent calculation methods (VASP and CASTEP) to identify the states of the H-bonds. According to Ref. [46], there are three kinds of H-bond states, Double Donor/DD (the two H atoms of a H_2O molecule both form H-bonds with two other O atoms of two neighboring H_2O molecules), Single Donor/SD (only one H-atom of a H_2O molecule forms an H-bond), and Non Donor/ND (none of the H atoms form H-bonds). From numerous calculations of X-ray absorption spectra (XAS) producing the intensities of pre-edge at 535 eV and main-edge at 537 eV for H_2O, Wernet et al. gave an empirical formula as a cut-off for formation of H-bond

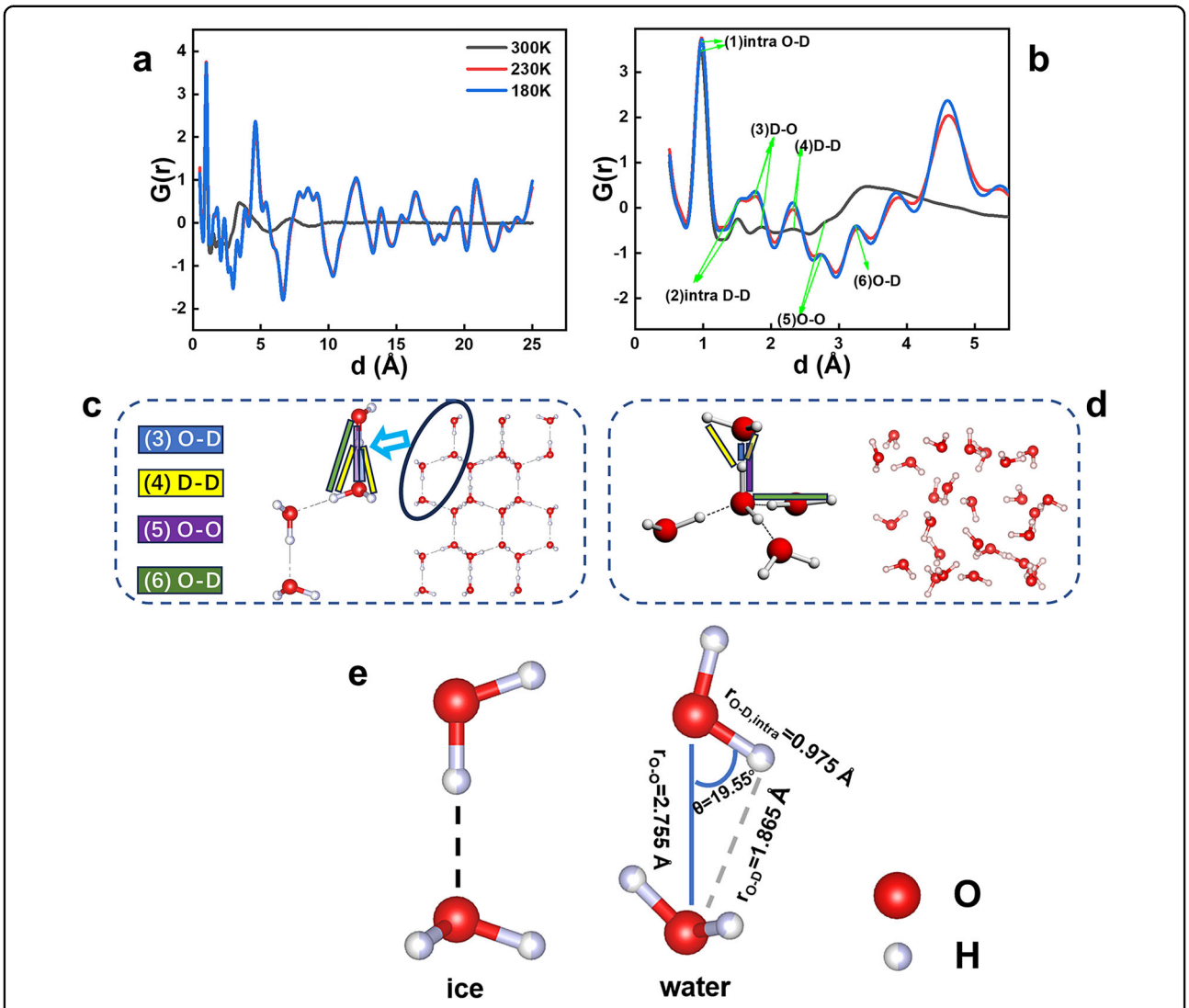

Fig. 4 Pair Distribution Function results obtained from neutron diffraction of D_2O. a PDF results obtained at 180, 230, and 300 K. **b** Enlarged view of the low distance area of **a**. Illustration of diverse atom pairs marked with different colors in **c** ice phase and **d** liquid water. Blue: (3) O-D, yellow: (4) D-D, and purple: (5) O-O. Right side shows four unit cells. (red ball and white ball denote O and H atom, respectively). **e** Illustration of the dynamics of two neighboring molecules from ice to water.

Table 1 Peak position at different temperatures in the PDF curves (Fig. 4b).

T/K	X peak's position/Å	(1) O-D	(2) D-D	(3) O-D	(4) D-D	(5) O-O
180		0.975	1.530	**1.765**	2.315	2.745
230		0.975	1.535	**1.765**	2.325	2.745
300		0.965	1.505	**1.865**	2.325	2.755
$\lvert\Delta d_{ice\text{-}water}\rvert$/Å		0.01	0.025	**0.1**	0.01	0.01

The first two peaks (1) and (2) correspond intramolecular pairs in a D_2O molecule, while (3), (4), and (5) correspond intermolecular pairs. Pair (3) has the largest elongation from ice to liquid water and is marked by bold characters.

(Supplementary Note S7)[46]:

$$r(\theta) = -0.00044\theta^2 + r_{max}, \quad (1)$$

where r(θ) stands for the O-O distance $r_{O\text{-}O}$ of two neighboring H_2O molecules in units of Å, θ for the O-O-H angle between the two neighboring molecules in units of degrees (Fig. 5a and b), and r_{max} for the cutoff value for the H-bond at θ = 0. The most essential issue during the simulation is to obtain an accurate r_{max}, which denotes the boundary between the two areas of intact and broken H-bonds (the vertex of the parabola, also in unit of Å, see Fig. 5a). As detailed above, two basic parameters

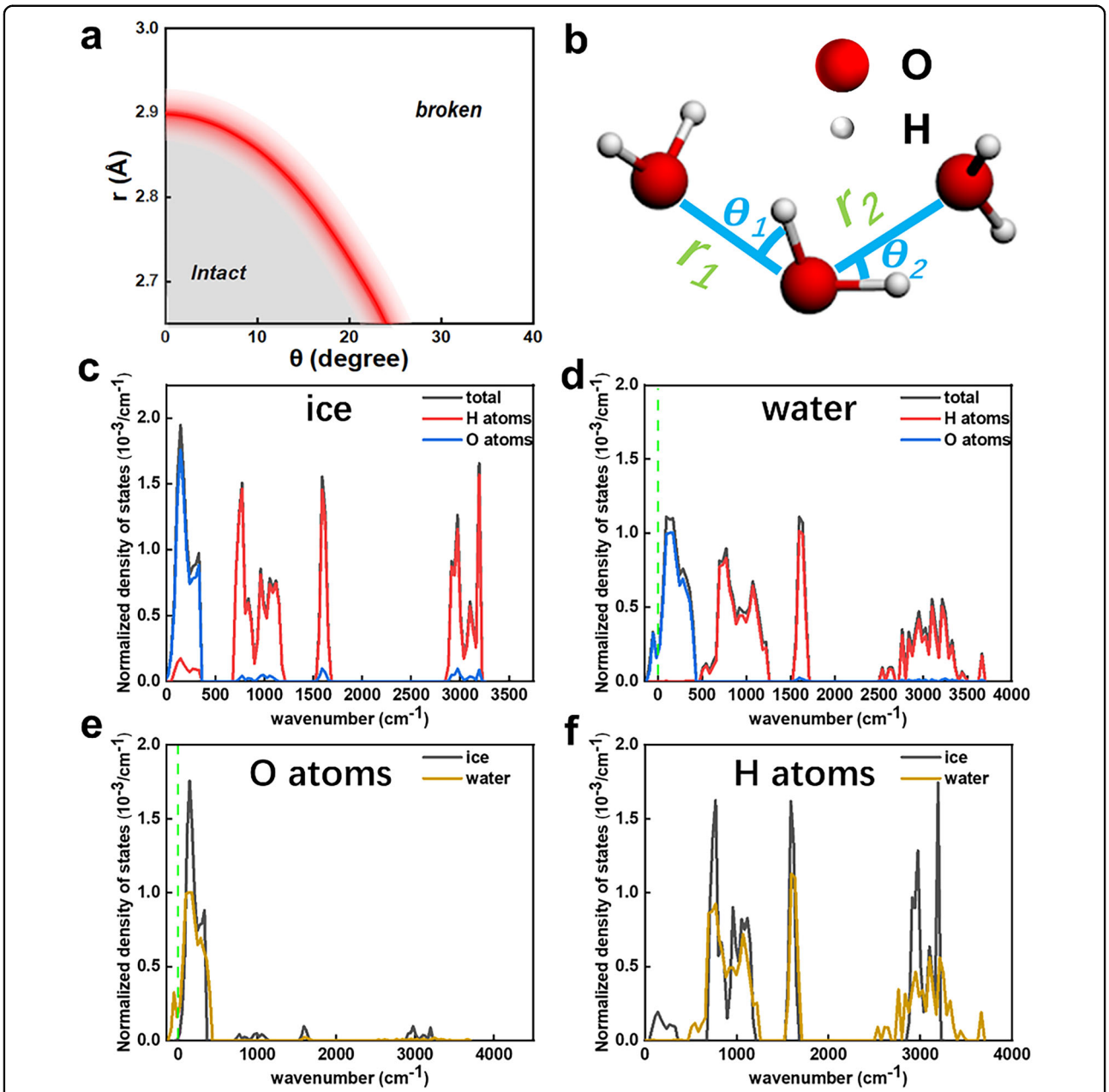

Fig. 5 Illustration of criterion parameters, cut off function, and phonon density of states (PDOS) spectra of H_2O. a Cut off function $r(\theta) = -0.000446^2 + r_{max}$ with $r_{max} \approx 2.9$ Å[46]. The shaded area denotes intact H-bonds and the other region represents broken ones. **b** Illustration of the (r, θ) between the two neighboring molecules defined in the simulation. The phonon density of states (PDOS) spectra of H_2O in **c** ice and **d** water at 298 K. **e** Contribution from O atoms and **f** from H atoms in PDOS. Green dashed line in **d** and **e** indicates the imaginary frequency in the calculation results of liquid water. The PDOS is calculated within the harmonic approximation at 0 K, which eventually leads to the occurrence of an imaginary frequency in the disordered water.

($r_{O\text{-}O}$, θ) = (2.755 Å, 19.55°) have been determined from PDF analysis. Substituting the values into the function (1), we can get the closest cutoff r_{max}~2.9 Å, which is always a vacancy in previous simulations[46]. In other words, this r_{max} used in the simulation can most exactly reflect the situations in realistic liquid water.

After exerting arbitrary perturbations on the ideal crystal ice structure for 9000 steps (9 ps) by VASP or CASTEP, we obtained a disordered, asymmetric structure of liquid water, from which the nearest neighboring O-O distances r_1 and r_2 and the corresponding O-O-H angles θ_1 and θ_2 illustrated in Fig. 5b were sorted and assigned as

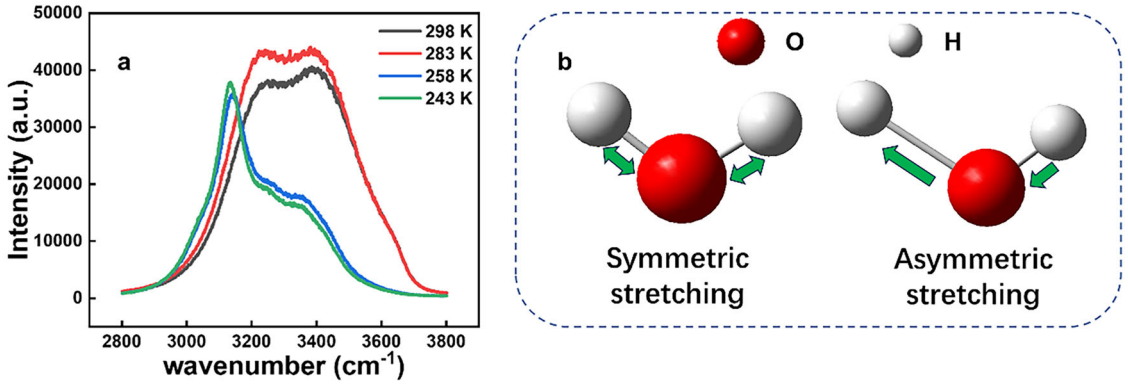

Fig. 6 Raman spectra and illustration of the OH-sb. a Raman spectra at four temperatures. **b** Illustration of symmetric stretching (both bonds elongate/contract simultaneously) and asymmetric stretching (one bond elongates/contracts while the other contracts/elongates), where red and white balls denote O and H atoms, respectively. (see detailed analysis given in Supplementary Note S8 and the last part of Movie S2).

intact or broken areas in Fig. 5a. The three kinds of H-bonds were then determined according to the obtained r_{max}~2.9 Å above and the criterion mentioned in Supplementary Note S7. Statistics presented the percentage of three types of H-bonds in water as follows: DD = 54.2%, SD = 40.3%, and ND = 5.5% based on VASP, and DD = 58.3%, SD = 37.5% and ND = 4.2% based on CASTEP. According to XAS experiments of H_2O[47], the energy difference between intact H-bonds in ice and broken H-bonds in water is 1.5 kcal/mol, from which we can calculate the enthalpy change ΔH during the ice-water phase transition. We then surprisingly found that the theoretical ΔH~357.9 J/g from VASP and ΔH~320.2 J/g from CASTEP are almost the same as the measured ΔH = 340 J/g by DSC, which strongly suggests the rationality of the obtained percentages of the three types of H-bonds in water. Accordingly, the average number of H-bonds ($N = 4 \times DD\% + 2 \times SD\% + 0 \times ND\%$) per H_2O molecule in liquid water can be determined (VASP: N~2.974/molecule and CASTEP: N~3.082/molecule), noting the $N = 4$ in ice because of the completely intact H-bonds (DD = 100%). That is to say, the coordination number of H-bonds changes from 4/H_2O molecule for ice to ~3/H_2O molecule for liquid water, which is the source of the huge entropy change across the ice-water transition. It should be noted that the obtained H-bonds number per H_2O molecule is only an equilibrium occasion in liquid water, the real-world circumstance is much more complicated with continuously broken and reformed H-bonds[57]. Here, for simplification, only the ice-water phase transition was focused ignoring the dynamic process of H-bonds in water.

Proceeding the simulation further, the phonon density of states (PDOS) reflecting the vibration information can be obtained, as illustrated in Fig. 5c-f. Overall, the PDOS spectra of both ice and water can be divided into four main regions: the vibrational/translational band below 500 cm^{-1}, the swagging band around 1000 cm^{-1}, the OH-bending band around 1600 cm^{-1}, and the OH-stretching band around 3000 cm^{-1}, as presented in Movie S2. The spectra are similar in the low frequency range with the spectrum of water being a little broadened with weaker peak intensity (Fig. 5c, d); however, the high wavenumber regions were notably different (2500–3500 cm^{-1}, as shown in Fig. 5c, d, which is also the main Raman spectrum range, as shown in Fig. 6a), where the peaks are more complex in the liquid water than in ice, reflecting that the water becomes more chaotic on transitioning from ice. To discuss the change of PDOS, we would then regard the ice as a network consisting of balls (molecules) with springs (H-bonds) connecting each molecule, with one side of the spring being linked by H and the other by O. As shown in Fig. 5e and f, the PDOS peaks of O and H in water decrease and widen on transitioning from ice, especially in the range of 0–1000 cm^{-1} for O and the whole range for H, reflecting the substantial change of H-bonds. In the ice form, H_2O molecules are tightly bonded with each other with the perfect springs' connection, i.e., Double Donor species of H-bonds dominate; hence, the location of a certain atom would be accurate, leading to some specific relative atom distances, which represents the corresponding peaks in the PDOS spectrum. In addition, if one molecule in this network is affected, the others would also be more or less influenced, which then would lead to the atoms' collective phenomenal vibration around a certain position at a similar frequency when a perturbation is applied in the ice system, presenting the pronounced and sharp PDOS intensity. In contrast, the H-bonds/springs are impaired in liquid water, i.e., the Single Donor and Non-Donor species emerge and the coordination number of H-bonds declines to ~3/molecule, so some springs are not capable enough

to bind the molecules at a certain location like the situation in ice and the correlation among molecules decreases. Therefore, the partial unbound H_2O molecules have a higher freedom; as such, the possible location of an atom would be difficult to determine, that is, numerous relative atom distances emerge, bringing about the broad, flat and messy PDOS spectrum and the bane of which is just the impairment of the numerous H-bonds once intact in original ice form.

Raman spectra

In a bit to understand the change of H-bonds during phase transition, we further measured Raman spectra which reflect the bond dynamics between atoms (Fig. 6a). There are three bands for H_2O in the Raman spectrum[60]: the translational bands below 400 cm^{-1}, the OH–bending bands around 1600 cm^{-1}, and the OH–stretching band (denoted as OH–sb) corresponding to the 2900–3700 cm^{-1} wavenumber region[60,61]. To simplify the issue, we focused on the OH-sb because this band is the most intense and easily affected by structural change[60].

In ice at 243 and 258 K, H bonds are steadily formed and consequently the H_2O molecules are more likely to elongate or contract simultaneously, producing isotropic expansion/shrinkage of macroscopic crystalline features, as reflected by the strong symmetric O-H stretching at 3130 cm^{-1}. The inferior asymmetric stretch at around 3350 cm^{-1} corresponds to anisotropic effects and is almost completely inhibited by the ordering in ice with strong H-bonds (Fig. 6a and b). As the temperature increases across T_C, both bands blue shift; however, the increased amplitude of the asymmetric band was much more pronounced than that of the symmetric band. In water at 283 K, the intensity of both become nearly the same, and the asymmetric band surpasses its counterpart at 298 K. This result provides evidence that water molecules become more individual with less correlation, i.e., they become freer and more disordered on account of the decrease in coordination number of H-bonds per molecule compared with those in ice (see detailed analysis given in Supplementary Note S8).

Discussion

The external perturbation driving an ice-water transition can be either temperature or pressure. From the well-accepted three-phase diagram of H_2O[51,55,56], the boundary between liquid water and hexagonal ice is approximately a straight line, i.e., the temperature and pressure have the same priority for determining the liquid/ice phase over a given temperature and pressure range ($T > -100$ °C and $P < 0.20$ GPa). That is, pressure plays the same role as temperature in driving the formation/breakage of H-bonds in H_2O, and the nature of the liquid/ice produced by either temperature or pressure is the same. Note that ice has a larger specific volume (1.09×10^{-3} m^3/kg) than liquid water ($1 \times 10^{-3} m^3/kg$), which creates a negative dT_c/dP in our barocaloric outcomes; therefore, applying pressure can drive the ice-water transition and hence produce a huge barocaloric effect.

One of the key issues in this work is the largely reduced hysteresis by adding 1.33 wt% $GdCl_3$ in pure H_2O. In general, the addition of any dopants, whether it is soluble or not, can reduce the supercooling degree in supercooled water, the mechanism behind is that the external dopants can provide an additional surface or carrier where H_2O molecules can adsorb, which can help or accelerate the nucleation process[51]. In addition, it can also reduce the energy barrier between the metastable supercooled state and stable ice form, just like the catalysis in the chemical reactions[62]. Specifically, the mechanism of reducing hysteresis in $GdCl_3$ doped H_2O can be explained as the Gd^{3+} and Cl^- ion would absorb H_2O molecules, or it can be expressed that H_2O molecules would adsorb on the surface of these ions, which improves the nucleation or crystal growth probability considerably than pure H_2O as well as lowering the energy barrier for freezing. Therefore, the supercooling degree is mediated.

To understand the mechanism of reduced supercooling degree by dopants, we performed sufficient experiments, and answered why we chose $GdCl_3$ as dopants (see details given in Supplementary Note S3). To find out the critical factors that influence supercooling, such as the charge, volume and solubility of the dopants' ions, we chose diverse dopants including monovalence ones: $AgNO_3$, CsI, and NH_4Cl, divalence ones: $CaCl_2$, $CoCl_2$, and $MgCl_2$, trivalence ones: $AlCl_3$, $GdCl_3$, $EuCl_3$, and $BiCl_3$, as well as insoluble dopants: graphite and TiO_2 (Fig. 2a), where $GdCl_3$ behaves the best. From detailed experiments and analysis (Supplementary Note S3), we summarized a rough regularity of the ideal dopants for reducing the hysteresis of pure H_2O, which may have the characters of larger ion volume, higher ion charge, larger ion magnetic moment and larger ion mass. However, the exact mechanism requires further research in corresponding field.

The colossal entropy change of H_2O reported here derives from the numerous H-bonds during the ice-water phase transition, which conveys robust enlightenment that H-bonds would enact an potent role to produce huge entropy change or latent heat in a system with first-order phase transition, even larger than the values observed in organic systems such as plastic crystals and solid-liquid phase transition n-alkanes. Note that the colossal entropy change of these organics is mainly from the changes of conformation ordering and/or molecular orientation. Therefore, H-bonds should be paid some attention in terms of searching for novel colossal BCE besides the well-known carbon chains. H-bond engineering could be used to introduce a potential colossal entropy change into

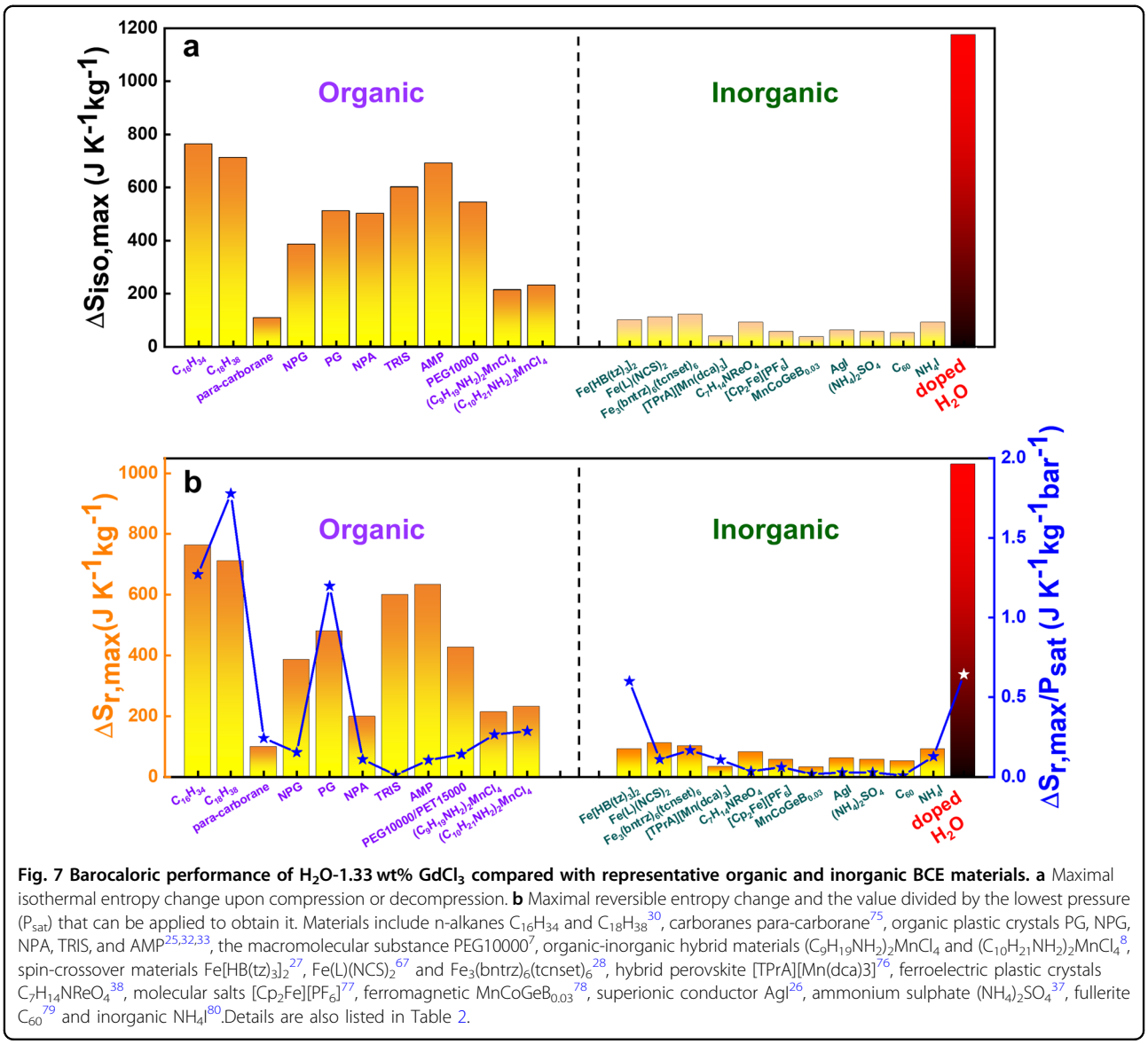

Fig. 7 Barocaloric performance of H_2O-1.33 wt% $GdCl_3$ compared with representative organic and inorganic BCE materials. a Maximal isothermal entropy change upon compression or decompression. **b** Maximal reversible entropy change and the value divided by the lowest pressure (P_{sat}) that can be applied to obtain it. Materials include n-alkanes $C_{16}H_{34}$ and $C_{18}H_{38}$[30], carboranes para-carborane[75], organic plastic crystals PG, NPG, NPA, TRIS, and AMP[25,32,33], the macromolecular substance PEG10000[7], organic-inorganic hybrid materials $(C_9H_{19}NH_2)_2MnCl_4$ and $(C_{10}H_{21}NH_2)_2MnCl_4$[8], spin-crossover materials $Fe[HB(tz)_3]_2$[27], $Fe(L)(NCS)_2$[67] and $Fe_3(bntrz)_6(tcnset)_6$[28], hybrid perovskite [TPrA][Mn(dca)3][76], ferroelectric plastic crystals $C_7H_{14}NReO_4$[38], molecular salts $[Cp_2Fe][PF_6]$[77], ferromagnetic $MnCoGeB_{0.03}$[78], superionic conductor AgI[26], ammonium sulphate $(NH_4)_2SO_4$[37], fullerite C_{60}[79] and inorganic NH_4I[80].Details are also listed in Table 2.

a target BCE product from the perspective of chemical synthesis. In general, to construct more powerful H-bond in a chemical complex, the acceptor side can be chosen to be F atoms because of its strongest electronegativity and hence an enhanced or robust H-bond can be achieved, which may require more external energy to overcome the energy barrier to complete the first-order phase transition and larger latent heat can be expected. Meanwhile, the energy of a H-bond also depends on the carrier or moiety where the acceptor (N, O, or F) and the donor H exist, i.e., the specific construction of the chemical complex such as bond categories, the chemical rings, etc. can also influence the strength of the target H-bonds[63,64], so the specific structure of the final product should be also considered to increase the strength. In addition, the idea to increase the number of H-bond in a certain complex during synthesis may also be feasible to create colossal entropy change via introducing more H atoms and corresponding N, O, and F atoms into the product. Combination of these ideas and consideration of these factors in H-bond engineering might lead to the invention of more effective BCE materials for the refrigeration field. Moreover, H-bonds can even be regarded as a certain "degree of freedom" just like others such as carbon chains in organic matters[7,8,65], the magnetism freedom in spin-crossover complexes[27–29,66,67], and the oriental order in plastic crystals[32] and so on. If the H-bonds and others co-exist in a system, the colossal entropy change would be further enhanced and the ideal BCE candidates may be born.

To evaluate the BCE properties of doped H_2O, we compared other materials that have a giant BCE, and the results are plotted in Fig. 7. The maximal isothermal ΔS_{iso}

of doped H_2O is absolutely the largest (ΔS_{iso}~1050 J·kg^{-1}·K^{-1}) among the listed materials whatever they are organic or inorganic, even more than 1.6 times that of the super-high value so far possessed by solid-liquid phase transition n-alkanes (ΔS~740 J·kg^{-1}·K^{-1})[30]. As for the practical-related reversible part, i.e., the reversible entropy change ΔS_r of doped H_2O is also large among reported BCE materials (Fig. 7b) at ΔS_r ~1018 J kg^{-1}·K^{-1}, which confirms the realistic prospects for its applications. The minimal pressure required to obtain the maximal reversible entropy change of doped H_2O is 0.16 GPa. To compare the practical BCE performance, we also define the parameter $\Delta S_{r,max}/P_{sat}$, where P_{sat} is the lowest pressure required to attain the highest reversible entropy change. As shown in Fig. 7a, b, the barocaloric performance of doped H_2O (either $\Delta S_{iso,max}$ or $\Delta S_{r,max}$ or $\Delta S_{r,max}/P_{sat}$) shows an absolute dominance in inorganic materials, and also largely superior to organic materials except the parameter $\Delta S_{r,max}/P_{sat}$ of solid-liquid phase transition n-alkanes and PG. As for the reversible refrigeration capacity RC_{rev}, a parameter representing capability to exchange the heat from hot to the cold end in an ideal cooling cycle, doped H_2O also shows superior position in either RC_{rev} or RC_{rev}/P among its peers as presented in Table 2 and Fig. S31 and S32. In inorganic materials, the BCE generally originating from crystal structural change is badly inferior to that of organic substances because the advantages of latter with carbon chains can bring about high structure flexibility due to complex conformational types and the ductility possessed by the chains. In contrast, the specific but simple inorganic H_2O full of H-bonds gets inverse. The contribution from the breakage/formation of H-bonds across ice-water transition makes H_2O show super colossal BCE performances, exceeding that of almost all organic materials and the harmful Freon commonly used in vapor compression refrigeration.

In conclusion, by resorting to the pressure-DSC, we quasi-directly measured and reported the colossal barocaloric effect in 1.33 wt% $GdCl_3$ doped H_2O. The reversible entropy change ΔS_r as large as ~1018 J kg^{-1} K^{-1} can be attained with a small hysteresis ~7.9 K under a low pressure of ~0.16 GPa and a value of 728 J kg^{-1} K^{-1} is detected at 0.1 GPa, which is so far the empyrean among all the reported barocaloric materials. The reversible refrigeration capacity RC_{rev} and the parameter RC_{rev}/P are also at the tier 1 position. Combining ND and PDF results, DFT-MD simulation, PDOS and Raman spectra measurements, the colossal thermal effect of H_2O is indicated from the breakage/formation of H-bonds across the ice-water transition. The coordination number of H-bonds changes from 4 H-bonds/molecule in ice to 3 H-bonds/molecule in liquid water, which essentially renders the conspicuous phase change and also the record-high entropy change; ultimately, super colossal thermal effect can be driven reversibly by low pressure, generating the reversible colossal barocaloric effect. Innately being safe, innocuous, environment-benign and ubiquitous, doped H_2O would be likely to be utilized as the coolant in the design strategy of balocaloric cooling system, probably opening a new era in the field of refrigeration in the future. In addition, the hint of the H-bonds bringing about colossal entropy change in H_2O also conveys the feasible method of H-bond engineering for the chemical synthesis to produce more attractive colossal entropy change in the target BCE candidates by creating stronger H-bonds and/or increasing the number of them, as well as even combining them with other degrees of freedom.

Methods

Materials

Sterile double-distilled water and the aforementioned dopants (Fig. 2) were all purchased from Maclin, Shanghai, China, and were used without further purification.

To reduce the supercooling degree, i.e., the hysteresis gap (see details given in Supplementary Note S3), doped H_2O was prepared as follows: first, a calculated amount pure liquid water, appropriate for the target mass ratio, was extracted with an injector and placed in a small sample vessel. Next, the selected dopants were added to the pure liquid water to generate a series of doped H_2O. After this procedure, these samples were measured by DSC to determine their corresponding hysteresis. The $GdCl_3$ doped H_2O had the smallest hysteresis (Fig. 2a), and different mass ratios of $GdCl_3$ were further explored to find the optimal concentration by pressure-DSC. The 1.33 wt% $GdCl_3$ doped one performed the best and was used for subsequent experiments (Fig. 2b).

Neutron diffraction (ND) measurements and PDF analysis

Neutron diffraction (ND) measurements were performed on the Time-of-Flight Multiple Physics Instrument (MPI) at the China Spallation Neutron Source (CSNS), which uses beam port 16# of the CSNS target station facing the center of a decoupled water moderator. To reduce the incoherent scattering background caused by H and increase the signal-to-noise ratio of coherent scattering, H_2O was substituted with D_2O. The MPI standard operating wavelength range was 0.1–4.5 Å. The beam cross-section center was 300 mm from the axis of the chopper. For the PDF measurements, the Q range was extended to a wide range of 0.08–100 Å^{-1} with a resolution of 0.4% by a physical design and the neutron flux at the sample was 10^7 s^{-1} cm^{-2}, thereby covering a multi-degree disorder and a multi-scale material with a good

Table 2 Barocaloric performance of H_2O-1.33 wt% $GdCl_3$ compared with representative organic and inorganic BCE materials.

	Compound	ΔS_{iso} ($J{\cdot}kg^{-1}{\cdot}K^{-1}$)	ΔS_r ($J{\cdot}kg^{-1}{\cdot}K^{-1}$)	P_{sat} (kbar)	$\Delta S_r/P_{sat}$ ($J{\cdot}kg^{-1}{\cdot}K^{-1}{\cdot}bar^{-1}$)	RC_{rev} ($J{\cdot}kg^{-1}$)	RC_{rev}/P ($J{\cdot}kg^{-1}{\cdot}GPa^{-1}$)	Ref.
organic	$C_{16}H_{34}$	762	762	0.6	1.27	5900 (0.1 GPa)	59000	[30]
	$C_{18}H_{38}$	711	711	0.4	1.7775	7800 (0.1 GPa)	78000	[30]
	Para-carborane	106.2	97.3	0.4	0.24325	1100 (0.06 GPa)	18333	[75]
	NPG	384	384	2.5	0.1536	6700 (0.57 GPa)	11754	[33]
	PG	510	479	0.4	1.1975	4500 (0.24 GPa)	18750	[33]
	NPA	500	197	1.8	0.10944	4500 (0.33 GPa)	13636	[33]
	TRIS	600	600	50	0.01198	0 (0.25 GPa)	0	[33]
	AMP	690	632	6	0.10533	0 (0.25 GPa)	0	[33]
	PEG10000/PET15000	543	426	3	0.142	3000 (0.4 GPa)	7500	[7]
	$(C_9H_{19}NH_2)_2MnCl_4$	212	212	0.8	0.265	1060 (0.1 GPa)	10600	[8]
	$(C_{10}H_{21}NH_2)_2MnCl_4$	230	230	0.8	0.2875	1150 (0.1 GPa)	11500	[8]
Inorganic	$Fe[HB(tz)_3]_2$	99	90	0.15	0.6	180 (0.015 GPa)	12000	[27]
	$Fe(L)(NCS)_2$	110	110	1	0.11	2500 (0.1 GPa)	25000	[67]
	$Fe_3(bntrz)_6(tcnset)_6$	120	100	0.6	0.16667	7200 (0.26 GPa)	27692	[28]
	[TPrA][Mn(dca)$_3$]	38	32	0.3	0.10667	66 (0.007 GPa)	9428	[76]
	$C_7H_{14}NReO_4$	90	80	2.3	0.03478	2700 (0.28 GPa)	9643	[38]
	$[Cp_2Fe][PF_6]$	55	55	0.9	0.06111	1050 (0.1 GPa)	10500	[77]
	$MnCoGeB_{0.03}$	35	30	1.7	0.01765	400 (0.48 GPa)	833	[78]
	AgI	60	60	2.2	0.02727	450 (0.25 GPa)	1800	[26]
	$(NH_4)_2SO_4$	55	55	2	0.0275	460 (0.25 GPa)	1840	[37]
	C_{60}	50	50	5.9	0.00847	4000 (0.59 GPa)	6780	[79]
	NH_4I	90	90	0.7	0.12857	1400 (0.08 GPa)	17500	[80]
	H_2O-1.33 wt%$GdCl_3$	**1050**	**1018**	**1.6**	**0.64375**	**9700 (0.19 GPa)**	**51052**	**This work[a]**

Isothermal entropy change (ΔS_{iso}), reversible entropy change (ΔS_r), Saturated pressure (P_{sat}), $\Delta S_r/P_{sat}$, reversible refrigeration capacity (RC_{rev}), and RC_{rev}/P are given.

resolution of the PDF in real space. Further details about the MPI have been previously reported[68,69]. The total neutron scattering data were processed using the Mantid software and Fourier transforms to obtain PDFs with a maximum momentum transfer $Q_{max} = 25\ Å^{-1}$. The full-profile Rietveld refinements of the ND patterns and the corresponding pair PDF were performed by FullProf and PDFgui software, respectively.

Raman spectra

Raman spectra were collected in backscattering geometry at variable temperatures by a Jobin Yvon T64000 triple spectrometer equipped with a cooled change-couple device. In the spectrometer a long focus objective of 20× magnification was used to focus the laser beam on the sample surface and to collect the scattered light. Raman spectra were excited with 532.0 nm radiation from a coherent solid-state laser. The laser power at the focus spot, approximately 1 μm in diameter, was maintained at 4.8 mW to obtain high quality spectra. A spectral resolution better than 1 cm^{-1} was obtained from our experimental configuration.

Pressure DSC, specific heat measurements and barocaloric effects

The measurement of heat flow was performed using the high-pressure differential scanning calorimeter (μDSC7 evo microcalorimeter from SETARAM, temperature range: −40~120 °C, pressure range: 0–0.1 GPa). The temperature ramping rate was set to be 1 K/min during the whole process of the heat flow measurement. High purity N_2 gas (99.999%) was used to apply hydrostatic pressure ranging from atmospheric pressure to 0.1 GPa. The specific heat capacity was also measured by the same calorimeter, the corresponding measurement was calibrated and tested against naphthalene (Standard for GC, ≥99.5% GC). In the formal measurement, a large amount of the sample (761 mg) was used to achieve the precise C_p baseline of both ice and water phases at ambient pressure (Supplementary Fig. S4 and Supplementary Note S1).

On the basis of the heat flow (Q) response of the temperature at variable pressure, the phase transition entropy curves were constructed by integration of the heat flow:

$$S_{pt}(T,P) = \int_{T_0}^{T} \frac{1}{T'} \frac{Q(T',P)}{\dot{T}'} dT'. \quad (2)$$

Considering the thermal response besides the latent heat of phase transition, the total entropy curves were constructed including the specific heat capacity contribution, where the specific heat capacity C_P at variable small pressures lower than 0.2 GPa was approximated as that for atmosphere pressure[24]:

$$S(T,P) = S_{pt}(T,P) + \int_{T_0}^{T} \frac{C_p}{T'} dT'. \quad (3)$$

The barocaloric isothermal entropy change curves (ΔS_{iso}) were obtained quasi-directly by isothermal subtraction of entropy curves at variable pressure: $\triangle S_{iso}(T, P_0 \rightarrow P_1) = S(T,P_1) - S(T,P_0)$. Specifically, the ΔS_{iso} for the pressurization process ($P_0 < P_1$) used *Q(T, P)* on heating, while the ΔS_{iso} for depressurization ($P_0 > P_1$) process used *Q(T, P)* on cooling. The reversible isothermal entropy change ΔS_r is the overlap of ΔS_{iso} between the pressurized and depressurized processes.

Barocaloric adiabatic temperature change curves (ΔT_{ad}) were obtained quasi-directly by adiabatic subtraction of entropy curves at variable pressure: $\triangle T_{ad}(T, P_0 \rightarrow P_1) = T(S,P_1) - T(S,P_0)$. Similar to ΔS_{iso}, the ΔT_{ad} for the pressurization process was determined by the entropy curves on heating and the ΔT_{ad} for depressurization process determined by the entropy curves on cooling. A reversible adiabatic temperature change ΔT_r was obtained from the adiabatic subtraction of the cooling entropy curve at atmospheric pressure and the heating entropy curve at the applied pressure[26].

Besides the entropy change involving the phase transition, the additional entropy change ΔS_+ caused by conventional thermal expansion and contraction under pressure were evaluated. The actual ΔS under pressure decreased slightly compared with the value, without considering conventional heat capacity. However, the result of the ΔS_+ for H_2O here is small, (3.7% out of 1170 J $K^{-1}kg^{-1}$ during heating and 1.3% of 1170 J $K^{-1}kg^{-1}$ in the cooling process, respectively) and would have little influence on the outcomes of this work. Notably, the water expansion coefficient α_{water} is nonlinear and up to 5.3×10^{-4}/K at above ~60 °C. Consequently, we evaluated $\Delta S_+ = 50$–65 J $K^{-1}kg^{-1}$ at 60–80°C away from phase transition, the magnitude of which appears to follow the same tread as the latent heat (see detailed analysis provided in Supplementary Note S8).

MD-DFT calculations on H-bonds and PDOS

Molecular dynamics (MD) simulations were carried out using the density functional theory (DFT) as implemented in the Vienna ab initio simulation package (VASP)[70] with the local density approximation (LDA)[71]. The valence states $2s^2 2p^4$ for O and $1s^1$ for H are used with an energy cutoff of 800 eV for the plane wave basis set. To yield the water structure, the hexagonal ice structure ($a = 4.4975$ Å and $c = 7.3224$ Å from our ND measurements), including four water molecules, was adopted. We performed ab initio molecular dynamics (AIMD) simulations based on VASP code in the canonical (NVT) ensemble with the Nosé thermostat[72] (SMASS = 3) at 273 and 298 K. The water structure data were taken over the last 9 ps (9000 steps) with a time step of 1 fs using a 3 × 3 × 2 hexagonal supercell (72 water molecules). All atomic positions are optimized with the conjugate gradient method until the total energy between two ionic steps are less than 10^{-6} eV and the atomic forces convergence criterion is set to -0.02 eV/Å. Similar AIMD simulations were also performed using the CASTEP code[73]. Moreover, the phonon density of states (PDOS) for ice with a 1 × 1 × 1 hexagonal cell and water with a 2 × 2 × 2

hexagonal supercell were calculated using the MedeA-phonon code[74].

After exerting arbitrary perturbations to the ideal crystal ice structure for 9000 steps (9 ps) by VASP or CASTEP, we obtained the disordered, asymmetric structure of liquid water, from which the nearest neighbor O-O distances r_1 and r_2 and the corresponding O-O-H angles θ_1 and θ_2 illustrated in Fig. 5b were sorted and assigned as intact or broken areas in Fig. 5a.

The H-bond coordination number was calculated as follows: After the structure of liquid water was constructed, the information of bond lengths and bond angles were subtracted from the structure. Next, the statistics were sorted and all ($r_{O\text{-}O}$, $\theta_{O\text{-}O\text{-}H}$) datasets were manually assigned to see whether they are in the shaded area, as shown in Fig. 5a. Finally, the three species: double donor/DD, single donor/SD and non-donor/ND were obtained from last step (detailed process, see Supplementary Note S6) and the average H-bond per H_2O molecule is calculated via $N = 4 \times \mathrm{DD}\% + 2 \times \mathrm{SD}\% + 0 \times \mathrm{ND}\%$.

Acknowledgements
This work was supported by the Science Center of the National Science Foundation of China (52088101), the National Key Research and Development Program of China (2023YFA1406003, 2021YFB3501202, 2020YFA0711500, the National Natural Sciences Foundation of China (92263202, U23A20550, 22361132534), the Strategic Priority Research Program B (XDB1270000) of Chinese Academy of Sciences (CAS), and the Synergetic Extreme Condition User Facility (SECUF).

Author details
[1]Beijing National Laboratory for Condensed Matter Physics, Institute of Physics, Chinese Academy of Sciences, Beijing, PR China. [2]School of Physical Sciences, University of Chinese Academy of Sciences, Beijing, PR China. [3]Songshan Lake Materials Laboratory, Dongguan, Guangdong, PR China. [4]Spallation Neutron Source Science Center, Dongguan 523803, China. [5]Institute of Solid State Chemistry, University of Science and Technology Beijing, 100083 Beijing, PR China. [6]Ganjiang Innovation Academy, Chinese Academy of Sciences, Ganzhou, Jiangxi 341000, China. [7]MOE Key Laboratory of Materials Physics and Chemistry under Extraordinary Conditions, Northwestern Polytechnical University, Xi'an 710072, China. [8]Ningbo Institute of Materials Technology & Engineering, Chinese Academy of Sciences, Ningbo, Zhejiang 315201, China

Author contributions
F.X.H. and B.G.S. formulated the project. Y.K. carried out the experiment and wrote the manuscript. J.T.W. performed the DFT-MD simulation. W.Y., L.H.H., and J.Z.H. collected neutron diffraction data. Y.K. and F.R.S. analyzed the data. Y.K. collected and analyzed the pressure calorimetry data. Y.K. and C.Q.J. collected and analyzed the Raman data. J.T.W. did the molecular dynamics simulation. Y.K. analyzed the simulation results. Y.K. and F.X.H. wrote the paper with input from all coauthors. Q.L. and Y.L.C. provided constructive viewpoints about the PDF results. Z.G.C. and B.S. participated the discussion about the MD simulation. J.W., Z.Y.T., B.J.W., Y.L., Y.Z.C., J.R.S., T.Y.Z., W.Z. and B.B.W. contributed to discussing and revising the paper.

Data availability
The main data supporting the findings of this study are available within the paper and its Supplementary Information. Considering the huge quantity of raw data, all raw data generated during the current study are available from the corresponding author (F.X.H. fxhu@iphy.ac.cn) upon request.

Code availability
Access to the DFT model codes is available on request from W.J.T (wjt@iphy.ac.cn).

Competing interests
The authors declare no competing interests.

Ethics approval and consent to participate
Ethics approval was not included since there is NO live vertebrates or human participant in all of our experiment in this work.

Publisher's note
Springer Nature remains neutral with regard to jurisdictional claims in published maps and institutional affiliations.

Supplementary information The online version contains supplementary material available at https://doi.org/10.1038/s41427-025-00619-2.

Received: 19 May 2025 Revised: 11 July 2025 Accepted: 14 August 2025
Published online: 03 October 2025

References

1. Purohit, P. et al. Electricity savings and greenhouse gas emission reductions from global phase-down of hydrofluorocarbons. *Atmos. Chem. Phys.* **20**, 11305–11327 (2020).
2. Stern, P. C. et al. Opportunities and insights for reducing fossil fuel consumption by households and organizations. *Nat. Energy* **1**, 16043 (2016).
3. McLinden, M. O., Brown, J. S., Brignoli, R., Kazakov, A. F. & Domanski, P. A. Limited options for low-global-warming-potential refrigerants. *Nat. Commun.* **8**, 14476 (2017).
4. Velders, G. J. M., Fahey, D. W., Daniel, J. S., McFarland, M. & Andersen, S. O. The large contribution of projected HFC emissions to future climate forcing. *Proc. Natl. Acad. Sci. USA* **106**, 10949–10954 (2009).
5. Henry, A., Prasher, R. & Majumdar, A. Five thermal energy grand challenges for decarbonization. *Nat. Energy* **5**, 635–637 (2020).
6. Mañosa, L. & Planes, A. Solid-state cooling by stress: a perspective. *Appl. Phys. Lett.* **116**, 050501 (2020).
7. Yu, Z. et al. Colossal barocaloric effect achieved by exploiting the amorphous high entropy of solidified polyethylene glycol. *NPG Asia Mater.* **14**, 96 (2022).
8. Gao, Y. et al. Reversible colossal barocaloric effect dominated by disordering of organic chains in $(CH_3–(CH_2)_{n-1}–NH_3)_2MnCl_4$ single crystals. *NPG Asia Mater.* **14**, 34 (2022).
9. Li, F., Li, M., Niu, C. & Wang, H. Atomic-scale insights into the colossal barocaloric effects of neopentyl glycol plastic crystals. *Appl. Phys. Lett.* **120**, 073902 (2022).
10. Niu, C. et al. Colossal barocaloric effect of plastic crystals imbedded in silicon frame near room temperature: Molecular dynamics simulation. *Appl. Phys. Lett.* **124**, 103905 (2024).
11. Xu, X. et al. General approach for efficient prediction of refrigeration performance in caloric materials. *Phys. Rev. Appl.* **22**, 014036 (2024).
12. Xu, X., Li, F., Niu, C., Li, M. & Wang, H. Machine learning assisted investigation of the barocaloric performance in ammonium iodide. *Appl. Phys. Lett.* **122**, 043901 (2023).
13. Li, F. et al. Predicting large comprehensive refrigeration performance of plastic crystals by compositing carbon architectures for room temperature application. *Appl. Phys. Lett.* **123**, 183902 (2023).
14. Li, F., Niu, C., Xu, X., Li, M. & Wang, H. The effect of defect and substitution on barocaloric performance of neopentylglycol plastic crystals. *Appl. Phys. Lett.* **121**, 223902 (2022).
15. Biswas, A. et al. Designed materials with the giant magnetocaloric effect near room temperature. *Acta Mater.* **180**, 341–348 (2019).
16. Terada, N. & Mamiya, H. High-efficiency magnetic refrigeration using holmium. *Nat. Commun.* **12**, 1212 (2021).
17. Guillou, F. et al. Non-hysteretic first-order phase transition with large latent heat and giant low-field magnetocaloric effect. *Nat. Commun.* **9**, 2925 (2018).
18. Wang, Y. et al. A high-performance solid-state electrocaloric cooling system. *Science* **370**, 129–133 (2020).
19. Nouchokgwe, Y. et al. Giant electrocaloric materials energy efficiency in highly ordered lead scandium tantalate. *Nat. Commun.* **12**, 3298 (2021).
20. Torelló, A. et al. Giant temperature span in electrocaloric regenerator. *Science* **370**, 125–129 (2020).

21. Lin, Y. et al. A full solid-state conceptual magnetocaloric refrigerator based on hybrid regeneration. *Innovation* **5**, 100645 (2024).
22. Tušek, J. et al. A regenerative elastocaloric heat pump. *Nat. Energy* **1**, 16134 (2016).
23. Hou, H. et al. Fatigue-resistant high-performance elastocaloric materials made by additive manufacturing. *Science* **366**, 1116–1121 (2019).
24. Moya, X., Kar-Narayan, S. & Mathur, N. D. Caloric materials near ferroic phase transitions. *Nat. Mater.* **13**, 439–450 (2014).
25. Lloveras, P., Aznar, A., Barrio, M., Negrier, Ph., Popescu, A. et al. Colossal barocaloric effects near room temperature in plastic crystals of neopentylglycol. *Nat. Commun.* **10**, 1803 (2019).
26. Aznar, A. et al. Giant barocaloric effects over a wide temperature range in superionic conductor AgI. *Nat. Commun.* **8**, 1851 (2017).
27. Seo, J., Braun, J. D., Dev, V. M. & Mason, J. A. Driving Barocaloric Effects in a Molecular Spin-Crossover Complex at Low Pressures. *J. Am. Chem. Soc.* **144**, 6493–6503 (2022).
28. Romanini, M. et al. Giant and reversible barocaloric effect in trinuclear spin-crossover complex $Fe_3(bntrz)_6(tcnset)_6$. *Adv. Mater.* **33**, 2008076 (2021).
29. Vallone, S. P. et al. Giant Barocaloric Effect at the Spin Crossover Transition of a Molecular Crystal. *Adv. Mater.* **31**, 1807334 (2019).
30. Lin, J. et al. Colossal and reversible barocaloric effect in liquid-solid-transition materials n-alkanes. *Nat. Commun.* **13**, 596 (2022).
31. Shuang, J. et al. Colossal barocaloric effect in encapsulated solid-liquid phase change materials. *Adv. Funct. Mater.* **35**, 2413924 (2025).
32. Li, B. et al. Colossal barocaloric effects in plastic crystals. *Nature* **567**, 506–510 (2019).
33. Aznar, A. et al. Reversible and irreversible colossal barocaloric effects in plastic crystals. *J. Mater. Chem. A* **8**, 639–647 (2020).
34. Li, F. B. et al. Understanding colossal barocaloric effects in plastic crystals. *Nat. Commun.* **11**, 4190 (2020).
35. Piper, S. L. et al. Organic ionic plastic crystals having colossal barocaloric effects for sustainable refrigeration. *Science* **387**, 56–62 (2025).
36. Tamarit, J.-L. & Lloveras, P. Compressed ionic plastic crystals are cool. *Science* **387**, 24–25 (2025).
37. Lloveras, P. et al. Giant barocaloric effects at low pressure in ferrielectric ammonium sulphate. *Nat. Commun.* **6**, 8801 (2015).
38. Salvatori, A. et al. Large barocaloric effects in two novel ferroelectric molecular plastic crystals. *J. Mater. Chem. A.* **11**, 12140–12150 (2023).
39. Meng, Q.-R. et al. An unprecedented hexagonal double perovskite organic–inorganic hybrid ferroelastic material: $(piperidinium)_2[KBiCl_6]$. *Chem. Commun.* **57**, 6292–6295 (2021).
40. Seo, J. et al. Colossal barocaloric effects with ultralow hysteresis in two-dimensional metal–halide perovskites. *Nat. Commun.* **13**, 2536 (2022).
41. Mañosa, L. et al. Giant solid-state barocaloric effect in the Ni–Mn–In magnetic shape-memory alloy. *Nat. Mater.* **9**, 478–481 (2010).
42. Mañosa, L. et al. Inverse barocaloric effect in the giant magnetocaloric La–Fe–Si–Co compound. *Nat. Commun.* **2**, 595 (2011).
43. Liu, K. et al. Microstructure and giant baro-caloric effect induced by low pressure in Heusler $Co_{51}Fe_1V_{33}Ga_{15}$ alloy undergoing martensitic transformation. *J. Mater. Sci. Technol.* **73**, 76–82 (2021).
44. Stern-Taulats, E. et al. Tailoring barocaloric and magnetocaloric properties in low-hysteresis magnetic shape memory alloys. *Acta Mater.* **96**, 324–332 (2015).
45. Cheng, P.-T. et al. Low-pressure-induced large barocaloric effect in $MnAs_{0.94}Sb_{0.06}$ alloy around room temperature. *Rare Met* **42**, 3977–3984 (2023).
46. Wernet, P. et al. The Structure of the First Coordination Shell in Liquid Water. *Science* **304**, 995–999 (2004).
47. Smith, J. D. et al. Energetics of Hydrogen Bond Network Rearrangements in Liquid Water. *Science* **306**, 851–853 (2004).
48. Al-Sayyab, A. K. S., Navarro-Esbrí, J., Barragán-Cervera, A., Kim, S. & Mota-Babiloni, A. Comprehensive experimental evaluation of R1234yf-based low GWP working fluids for refrigeration and heat pumps. *Energy Convers. Manag.* **258**, 115378 (2022).
49. Conte, R., Azzolin, M., Bernardinello, S. & Del Col, D. Experimental investigation of large scroll compressors working with six low-GWP refrigerants. *Therm. Sci. Eng. Prog.* **44**, 102043 (2023).
50. Makhnatch, P., Mota-Babiloni, A., López-Belchí, A. & Khodabandeh, R. R450A and R513A as lower GWP mixtures for high ambient temperature countries: Experimental comparison with R134a. *Energy* **166**, 223–235 (2019).
51. Akyurt, M., Zaki, G. & Habeebullah, B. Freezing phenomena in ice–water systems. *Energy Convers. Manag.* **43**, 1773–1789 (2002).
52. Vonnegut, B. The Nucleation of Ice Formation by Silver Iodide. *J. Appl. Phys.* **18**, 593–595 (1947).
53. Hozumi, T., Saito, A., Okawa, S. & Matsumura, T. Effect of bubble nuclei on freezing of supercooled water. *Int. J. Refrig.* **25**, 243–249 (2002).
54. Watanabe, K. Relationship between growth rate and supercooling in the formation of ice lenses in a glass powder. *J. Cryst. Growth* **237–239**, 2194–2198 (2002).
55. Lobban, C., Finney, J. L. & Kuhs, W. F. The structure of a new phase of ice. *Nature* **391**, 268–270 (1998).
56. Chou, I.-M., Blank, J. G., Goncharov, A. F., Mao, H. & Hemley, R. J. In Situ Observations of a High-Pressure Phase of H_2O Ice. *Science* **281**, 809–812 (1998).
57. Fecko, C. J., Eaves, J. D., Loparo, J. J., Tokmakoff, A. & Geissler, P. L. Ultrafast Hydrogen-Bond Dynamics in the Infrared Spectroscopy of Water. *Science* **301**, 1698–1702 (2003).
58. Urbic, T. & Dill, K. A. Water Is a Cagey Liquid. *J. Am. Chem. Soc.* **140**, 17106–17113 (2018).
59. Rahman, A. & Stillinger, F. H. Hydrogen-bond patterns in liquid water. *J. Am. Chem. Soc.* **95**, 7943–7948 (1973).
60. Đuričković, I. et al. Water–ice phase transition probed by Raman spectroscopy. *J. Raman Spectrosc.* **42**, 1408–1412 (2011).
61. Xue, X., He, Z. & Liu, J. Detection of water–ice phase transition based on Raman spectrum. *J. Raman Spectrosc.* **44**, 1045–1048 (2013).
62. Heneghan, A. F. & Haymet, A. D. J. Liquid-to-crystal heterogeneous nucleation: bubble accelerated nucleation of pure supercooled water. *Chem. Phys. Lett.* **368**, 177–182 (2003).
63. Meng, Y. et al. Boosting the humidity resistance of nonconventional luminogens with room temperature phosphorescence *via* enhancing the strength of hydrogen bonds. *J. Mater. Chem. C.* **9**, 8515–8523 (2021).
64. Naskar, S., Mishra, D., Butcher, R. J. & Chattopadhyay, S. K. Crystal engineering with aroyl hydrazones of diacetyl monooxime – Molecular and supramolecular structures of two Ni(II) and two Zn(II) complexes. *Polyhedron* **26**, 3703–3714 (2007).
65. Gao, Y.-H. et al. Low pressure reversibly driving colossal barocaloric effect in two-dimensional vdW alkylammonium halides. *Nat. Commun.* **15**, 1838 (2024).
66. Ohkoshi, S. et al. Giant adiabatic temperature change and its direct measurement of a barocaloric effect in a charge-transfer solid. *Nat. Commun.* **14**, 8466 (2023).
67. Seredyuk, M. et al. Reversible Colossal Barocaloric Effect of a New Fe^{II} Molecular Complex with Low Hysteretic Spin Crossover Behavior. *Adv. Funct. Mater.* **34**, 2315487 (2024).
68. Xu, J. et al. Multi-physics instrument: Total scattering neutron time-of-flight diffractometer at China Spallation Neutron Source. *Nucl. Instrum. Methods Phys. Res. Sect. Accel. Spectrometers Detect. Assoc. Equip.* **1013**, 165642 (2021).
69. Xu, J. et al. Physical design of multipurpose physics neutron diffractometer for the CSNS. *Nucl. Instrum. Methods Phys. Res. Sect. Accel. Spectrometers Detect. Assoc. Equip.* **927**, 161–168 (2019).
70. Kresse, G. & Furthmüller, J. Efficient iterative schemes for ab initio total-energy calculations using a plane-wave basis set. *Phys. Rev. B* **54**, 11169–11186 (1996).
71. Ceperley, D. M. & Alder, B. J. Ground State of the Electron Gas by a Stochastic Method. *Phys. Rev. Lett.* **45**, 566–569 (1980).
72. Nosé, S. A unified formulation of the constant temperature molecular dynamics methods. *J. Chem. Phys.* **81**, 511–519 (1984).
73. Clark, S. J. et al. First principles methods using CASTEP. *Z. Für Krist. - Cryst. Mater.* **220**, 567–570 (2005).
74. Parlinski, K., Li, Z. Q. & Kawazoe, Y. First-Principles Determination of the Soft Mode in Cubic ZrO_2. *Phys. Rev. Lett.* **78**, 4063–4066 (1997).
75. Zhang, K. et al. Colossal Barocaloric Effect in Carboranes as a Performance Tradeoff. *Adv. Funct. Mater.* **32**, 2112622 (2022).
76. Bermúdez-García, J. M. et al. Giant barocaloric effect in the ferroic organic-inorganic hybrid $[TPrA][Mn(dca)_3]$ perovskite under easily accessible pressures. *Nat. Commun.* **8**, 15715 (2017).
77. García-Ben, J. et al. A. Unveiling barocaloric potential in organometallic-sandwich compounds $[Cp_2M][PF_6]$ (M: Fe^{3+}, Co^{3+}). *J. Mater. Chem. A* **12**, 23751–23760 (2024).
78. Aznar, A. et al. Giant and Reversible Inverse Barocaloric Effects near Room Temperature in Ferromagnetic $MnCoGeB_{0.03}$. *Adv. Mater.* **31**, 1903577 (2019).
79. Li, J. et al. Reversible barocaloric effects over a large temperature span in fullerite C_{60}. *J. Mater. Chem. A* **8**, 20354–20362 (2020).
80. Ren, Q. et al. Ultrasensitive barocaloric material for room-temperature solid-state refrigeration. *Nat. Commun.* **13**, 2293 (2022).